



**HAL**  
open science

## Self-potential signals associated with preferential groundwater flow pathways in sinkholes

Abderrahim Jardani, Jean-Paul Dupont, A. Revil

► **To cite this version:**

Abderrahim Jardani, Jean-Paul Dupont, A. Revil. Self-potential signals associated with preferential groundwater flow pathways in sinkholes. *Journal of Geophysical Research: Atmospheres*, 2006, 111, pp.B09204. 10.1029/2005JB004231 . hal-00734717

**HAL Id: hal-00734717**

**<https://hal.science/hal-00734717>**

Submitted on 3 May 2021

**HAL** is a multi-disciplinary open access archive for the deposit and dissemination of scientific research documents, whether they are published or not. The documents may come from teaching and research institutions in France or abroad, or from public or private research centers.

L'archive ouverte pluridisciplinaire **HAL**, est destinée au dépôt et à la diffusion de documents scientifiques de niveau recherche, publiés ou non, émanant des établissements d'enseignement et de recherche français ou étrangers, des laboratoires publics ou privés.

## Self-potential signals associated with preferential groundwater flow pathways in sinkholes

A. Jardani,<sup>1,2</sup> J. P. Dupont,<sup>1</sup> and A. Revil<sup>3</sup>

Received 20 December 2005; revised 31 March 2006; accepted 27 April 2006; published 15 September 2006.

[1] Two self-potential (SP) surveys have been conducted at a test site located in Normandy, in the northwest of France, in a chalk karst in spring and summer 2005. The spring survey showed circular negative SP signals associated with the position of sinkholes and crypto-sinkholes, while the survey conducted during the summer showed fewer anomalies with lesser magnitudes. The negative SP anomalies observed in the spring survey were several tens of millivolts less than a reference located outside the ridge along which the sinkholes are located. In addition to the SP surveys, we also performed a DC electrical resistivity survey. The electrical resistivity tomogram shows the position of the interfaces between the chalk and the overlying clay with flint and loess covers and the position of the sinkholes. A linear relationship is observed between the SP signals and the thickness of the loess layer. In addition, large negative SP anomalies are associated with the sinkholes themselves. These SP signals are explained by solving the boundary value problem for the coupled hydroelectric problem. We fixed the boundary condition at the ground surface in terms of hydraulic flux associated with the infiltration of the meteoric water and a no-flow condition on the vertical boundaries. A finite element numerical simulation of this coupling is performed, and a fairly good agreement is obtained between the simulation and the observed SP signals. We show for the first time how the SP signals reflect mainly the topography of the clay with flint/loess interface and help to identify the location of sinkholes. Three-dimensional tomography algorithms are proposed to locate the source of these self-potential signals in the ground.

**Citation:** Jardani, A., J. P. Dupont, and A. Revil (2006), Self-potential signals associated with preferential groundwater flow pathways in sinkholes, *J. Geophys. Res.*, *111*, B09204, doi:10.1029/2005JB004231.

### 1. Introduction

[2] Leaching and runoff from agricultural areas are responsible for the contamination of the groundwater by nitrogen and pesticides. In chalk karstic areas, this is a real problem as sinkholes represent preferential fluid flow pathways that allow fast contamination of shallow aquifers from agricultural sources [Panno and Kelly, 2004]. In karstic areas, sinkholes are clustered along characteristic structural features such as structural lows and ridges that channel groundwater flow. The sinkholes have usually surface expression corresponding to more or less circular or elliptic depressions of the ground surface. However, some sinkholes are not mature enough to be visible at the ground surface, and they are only characterized by a network of fractures/conduits in the ground. These sinkholes are named crypto-sinkholes in this paper.

[3] Several geophysical methods have been used in the past to detect sinkholes. They include high-resolution gravimetry [Closson *et al.*, 2003], ground-penetrating radar, electromagnetic investigations, and DC resistivity tomography [van Schoor, 2002; Ahmed and Carpenter, 2003]. Gravimetry requires a strong density contrast between the chalk and the overburden. This method detects only large sinkholes or those located close to the ground surface but cannot be used to track the presence of crypto-sinkholes because the presence of a network of open conduits does not provide a strong perturbation of the gravity field. Ground-penetrating radar cannot be used if the overburden is conductive, e.g., in presence of a clay-rich cover like in the present study where a clay with flint cover is observed. DC electrical resistivity cannot be used to survey large regions due to the time needed for the acquisition of the data. In addition, electrical resistivity from DC or electromagnetic investigations is not sensitive to the direction of groundwater flow or to the hydraulic head distribution.

[4] This paper investigates the possibility of mapping sinkholes and crypto-sinkholes with the self-potential method. The self-potential method consists in the passive measurement of the electrical potential distribution at the ground surface or possibly in boreholes resulting from polarization phenomena in the ground. The self-potential signals are mapped with nonpolarizable electrodes. "Self-

<sup>1</sup>UMR 6143 Morphodynamique Continentale et Côtière, CNRS, Département de Géologie, Université de Rouen, Rouen, France.

<sup>2</sup>Bureau d'Etudes, Alise Environnement, Saint Jacques-sur-Darnétal, France.

<sup>3</sup>Equipe Hydrogéophysique et Milieux Poreux, CNRS, CEREGE, Université Paul Cézanne, Aix-en-Provence, France.

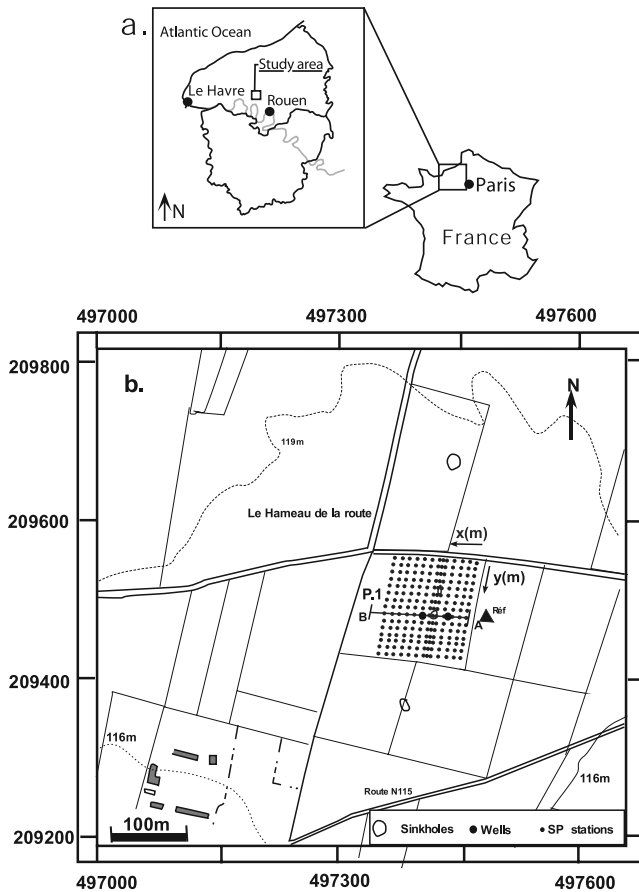


**Figure 1.** Position of the test site. (a) The test site is located in Normandy, in the northwest of France, near the city of Rouen. (b) Position of the self-potential (SP) stations, Ref represents the reference station for the self-potential measurements, and P1 corresponds to the trace of the electrical resistivity survey. Note that the sinkholes are organized along a north-south trend.

potential anomalies” correspond to spatial variations of the self-potential with respect to a baseline or a fixed reference placed outside the perturbed area. Self-potentials are the result of redox potential gradients (electroredox potential), chemical potential gradients (diffusion potential), temperature gradients (thermoelectric potential) in the ground. They can also be associated to the flow of the pore water in a porous material (streaming potential) [Fournier, 1989; Aubert et al., 1990, 1991; Aubert and Yéné Atangana, 1996]. For porous rocks, the underlying physics of this process has been reviewed by Ishido and Mizutani [1981], Revil et al. [1999], and Revil et al. [2004, and references therein] (see also Finizola et al. [2002, 2003] for applications to the hydrogeology of volcanic edifices).

[5] Sinkholes are associated with preferential groundwater flow in the ground, which, in turn, favors the dissolution of the carbonate substratum. Therefore the presence of sinkholes has an impact on the distributions of the hydraulic heads and hence on the occurrence of the self-potential signals. In limestones and chalks, past studies [e.g., Lange, 1999, and references therein] have shown correlations between self-potential anomalies and the presence of cavi-

ties. Gurk and Bosch [2001] suggested that the roof of karstic caves can be located from self-potential measurements at the ground surface using the method proposed by Aubert et al. [1990, 1991]. However, as far as we know, there are no published examples that use the self-potential method to locate sinkholes and therefore no study or numerical investigations of the potential of establishing a relationship between sinkholes and their associated self-potential anomalies.

[6] In most of the past studies, the self-potential method has been considered as a qualitative method, and practitioners did not attempt to quantify the geometry and density of the causative source. In this paper, we propose a quantitative interpretation of the self-potential signals to locate sinkholes and crypto-sinkholes. To reach this goal, we look for a physical explanation of the observed self-potential signals combining laboratory measurements, an electrical resistivity survey, and a finite element modeling of the coupled hydroelectric problem.

## 2. Field Survey

### 2.1. Geology

[7] Our test site corresponds to an agricultural area located in Normandy, in the chalk karst of the western Paris basin in an area of extensive agriculture practices (Figures 1 and 2). In this area, there is a thick chalk formation in which sinkholes are frequent [Laignel et al., 2004, and references therein]. The chalk substratum is overlain by clay with flint and loess covers. The overburden is derived from the alteration of the chalk layer itself (Figure 3). The thickness of this cover is from few meters to 10 m outside of sinkholes and as much as 15 m over some sinkholes. The

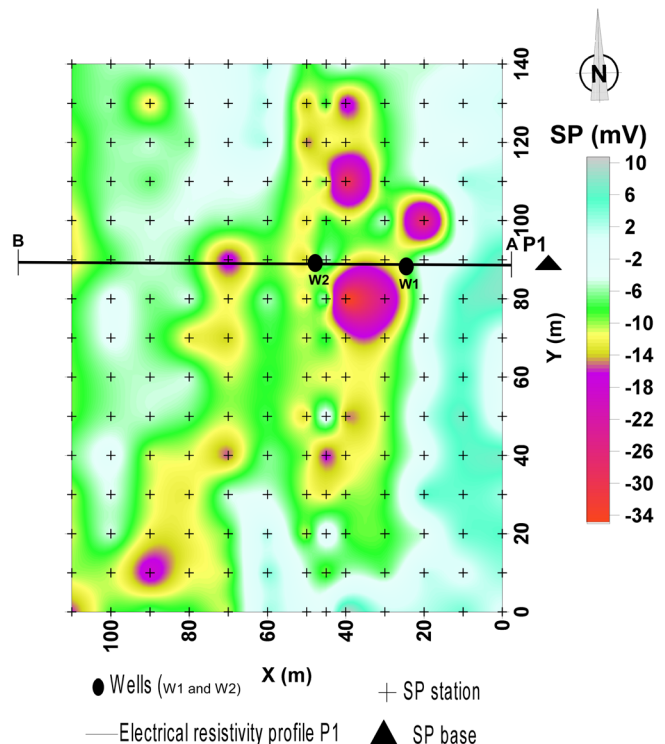


**Figure 2.** Self-potential map, position of the measurement stations, and position of the two boreholes (spring data).

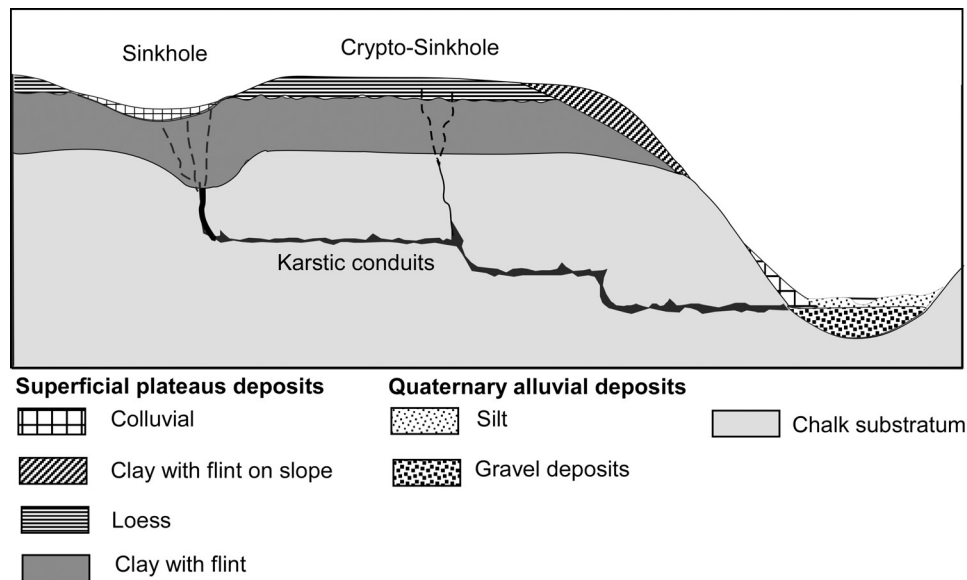


**Figure 3.** Geological cross section showing the presence of a sinkhole and a crypto-sinkhole (modified from *Laignel et al.* [2004]). The sinkholes are associated with a depression of the ground surface while there is no evidence, at the ground surface, of the existence of a crypto-sinkhole.

permeability of the cover is relatively low, typically  $\sim 5 \times 10^{-8} \text{ m s}^{-1}$  for the loess cover to  $10^{-10} \text{ m s}^{-1}$  for the clay with flint [*Brouyères et al.*, 2004]. Sinkholes favor the fast penetration of the water from the ground surface to the aquifer and the contamination of the aquifers with nitrates and herbicides. The main aquifer is located at a depth of 32 m, inside the chalk formation, and is used as a source of drinkable water.

[8] Several sinkholes are observable at the ground surface (Figure 1). They correspond to circular or elliptic depressions of the ground surface throughout the investigated area (Figure 3). However, the geomorphology of this plain does not always evidence the presence of sinkholes and the risk of potential collapses associated with their presence. Every year, houses and buildings are damaged because of the deformation of the ground associated to the presence of sinkholes in their vicinity. This points out the urge of detection tools to draw geohazard maps. Electrical resistivity and self-potential could be combined for that purpose.

## 2.2. Acquisition of the Data

[9] Measurements of the self-potential were performed with a high-input-impedance ( $10 \text{ M}\Omega$ ) voltmeter (Metrix MX20) and two nonpolarizable electrodes. The resolution of the voltmeter is 0.1 mV. The internal impedance of the voltmeter has to be much higher than the impedance between the electrodes to perform correct self-potential measurements [*Gex*, 1977; *Corwin and Hoover*, 1979] because of the small bias current used to measure the desired potential. This is the case in the present survey.

[10] The electrodes used for the SP survey were nonpolarizable Cu/CuSO<sub>4</sub> electrodes also called porous pots by practitioners. We used copper electrodes suspended in a supersaturated solution of copper sulfate inside a porous container. Large errors may develop from the use of steel electrodes [*Corwin and Hoover*, 1979], and Petiau (Pb/PbCl<sub>2</sub>) electrodes have been developed for long-term mon-

itoring because of their very small drift over period of several years. One of the electrodes is used as a fixed reference and is located outside the area along which the visible sinkholes are located (Figures 1 and 2). The reference electrode was setup in a hole, which was filled with a salted bentonite mud. Because the Cu/CuSO<sub>4</sub> electrodes are sensitive to temperature changes ( $1.2 \text{ mV}/^\circ\text{C}$ ), it is very important to reach thermal equilibrium between the porous pot and the surrounding soil before to start the measurements. This takes usually less than 10 min. The traveling electrode is used to scan the electrical potential at the ground surface to map the self-potential anomalies. For each measurement, a small hole (10 cm deep) was dug into the ground and filled with the same salted bentonite than used for the reference electrode. The use of salted bentonite help (1) to reduce the effect of the moisture variations in the soil during the measurements, (2) to average the measurements over a larger volume than only the one corresponding to the contact between the electrode and the ground, and (3) to improve the electrical contact between the electrode and the ground, that is, to decrease the contact impedance of the electrode/soil interface. Some practitioners still believe that the use of bentonite creates an additional spurious potential to the measured self-potential. This is not correct as the potential drop due to the salted bentonite cancels in the circuit between the reference electrode and the traveling electrode.

[11] The distance between measurement points was 10 m, but in the places where anomalous negative signals are recorded, we decrease the spacing between the measurements stations to 5 m (Figure 2). A total of 225 measurements were performed over a surface area of 15,400 m<sup>2</sup>. The error on the data was assessed on the following way. The reference was placed somewhere in the field and the scanning electrode was used 50 m away. A total of 15 measurements were performed over 1 m<sup>2</sup>. The error of these measurements was found to be  $2\sigma = 0.8 \text{ mV}$ . The

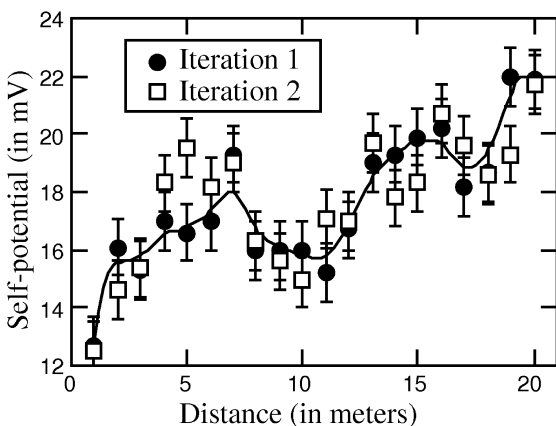


**Figure 4.** Repeatability of the self-potential measurements. Over short period of times (3 hours here), the reiteration of the same profile provides essentially the same pattern of self-potential measurements (date of the measurements 22 March 2006). The high values of the self-potential data shown here are coming from the fact that these data have not been corrected for the initial value of the static potential between the reference electrode and the traveling electrode.

repeatability was assessed by repeating twice a short SP profile during the same day. The result is shown Figure 4. It is clear that the self-potential data show a very good repeatability at this site.

[12] A resistivity survey was performed along a profile that is perpendicular to the small north-south valley along which the sinkholes are observed (Figure 1). For this survey, we used the Syscal Junior apparatus from IRIS instrument with a total of 48 electrodes. We used the Wenner- $\alpha$  array that consists of four aligned electrodes with intervals of  $a = 3$  m in our case. In this case the geometric factor of the array is equal to  $a$ , and the apparent resistivity is given by  $\rho_a = 2\pi a \delta\psi / I$ , where  $\delta\psi$  is the measured potential difference and  $I$  is the injected current. The Wenner- $\alpha$  array is used to distinguish between the various geological units in order to get a good idea of their respective resistivity and position. The pseudosection of apparent resistivity was inverted using the software RES2DINV developed by Loke and Barker [1996] using the L2 norm to minimize the cost function. We trust the quality of this resistivity survey because of (1) the very low contact impedance between the electrode and the ground (that allows to inject high currents), (2) the very low standard deviations associated with the measurements (few percent), and (3) the very low misfit error at the fourth iteration in the inversion of the apparent resistivity data (1.25%). In addition, we will show that the architecture of the ground determined from this survey is in agreement with drilling information.

### 3. Interpretation of Field Data

#### 3.1. Infiltration in the Vadose Zone

[13] Two self-potential surveys were performed at the test site described above in spring 2005 and in summer 2005 (Figure 5). In Normandy, spring is a rainy season (the rainfall will be discussed later in the modeling section).

The second survey was performed after an usual period of dryness in France. The map of the self-potential signals constructed from the spring data exhibits clear negative self-potential anomalies of few mV to approximately  $-30$  mV. The anomalies show two ridges along which more or less circular and strong (few tens of mV) self-potential anomalies are located. These anomalies cannot be associated here to lateral changes in soil types as the soil remains the same over the investigated area. However, the ridges are filled with loess as shown by drilling. Buried stream channels, richer in sand, provide a contrast to clay with flint deposits. Most of these negative anomalies were located along the trend where some sinkholes were identified from surface features. Because these ridges channel high volumes of groundwater flow, this is not surprising that the sinkholes are organized along these ridges.

[14] The self-potential map made in spring seems to reflect the topography of the substratum, but a quantitative analysis of this relationship is needed. We will demonstrate later that this map is actually the sum of two contributions: (1) a contribution associated with the thickness of the loess layer and (2) strong negative self-potential signals associated with the downward percolation of water in sinkholes and crypto-sinkholes.

[15] The idea that slow percolation of water through the vadose zone could be responsible for self-potential signals at the ground surface of the Earth was first proposed by

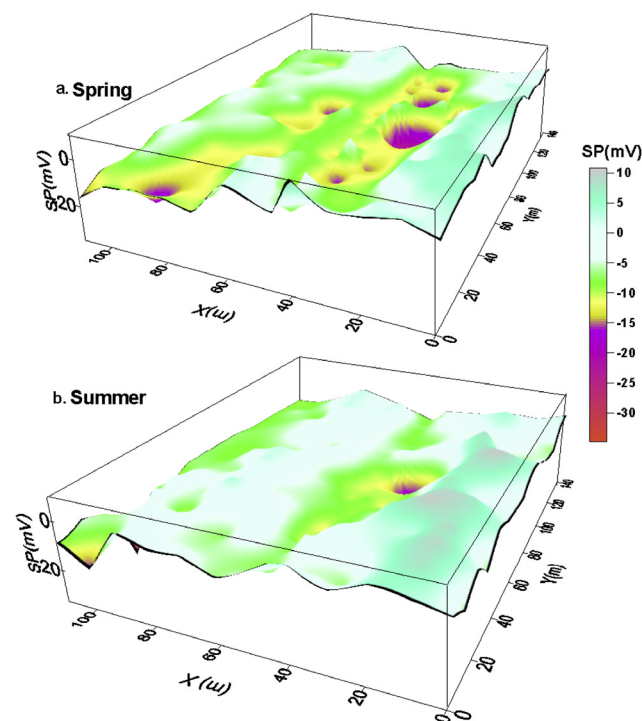


**Figure 5.** Self-potential surveys conducted in (a) spring (March) and (b) summer (August) 2005. In spring, the negative anomalies in the self-potential map are organized along two ridges. The topography of the ground surface is very small ( $<2$  m). It seems that the self-potential map reflects mainly the topography of the interface between the loess and the clay with flint cover.

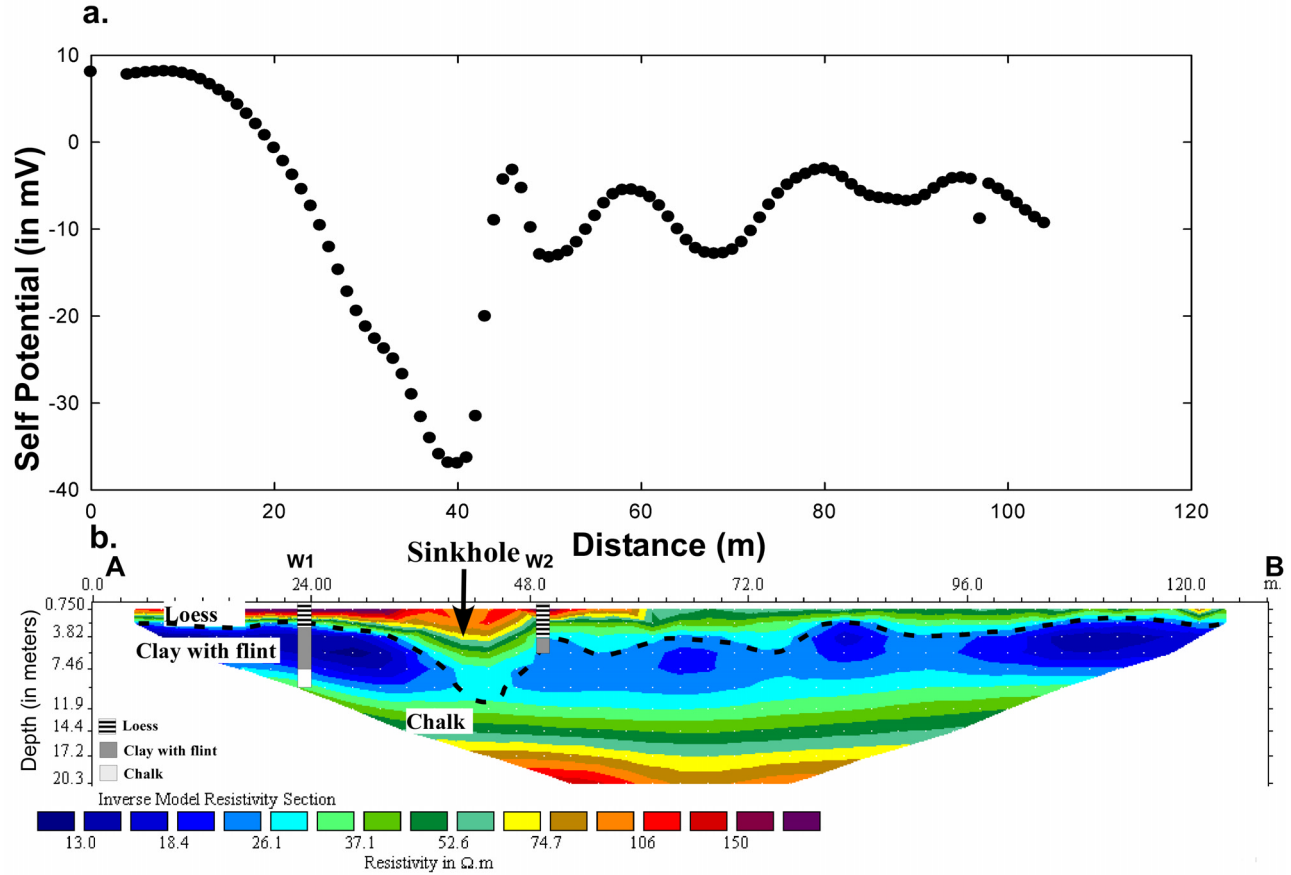


**Figure 6.** High-resolution self-potential profile along electrical resistivity profile P1 (electrode spacing of 3 m, Wenner- $\alpha$  array). We show the electrical resistivity tomography at the fourth iteration (RMS error 1.25%). The well is used to validate the electrical resistivity tomogram and to choose the electrical resistivity value used to draw the interface between the loess cover and the clay formation. This interface is indicated by the dashed line.

Zablocki [1978] and Jackson and Kauahikaua [1987] for volcanic areas. They assumed that self-potential data were mainly related to the distance along which water percolates vertically through the vadose zone before reaching the water table. In our case, this assumption may seem questionable but we will show in Appendix A that the Aubert's model can be derived from different assumptions. The empirical model of Zablocki was further conceptualized by M. Aubert and coworkers [Aubert et al., 1990, 1991; Aubert and Yéné Atangana, 1996; Boubekraoui and Aubert, 1999; Zhang and Aubert, 2003]. This is the so-called SPS model.

[16] We denote  $z(x, y)$  the topography of the ground and  $h(x, y)$  the topography of the clay-with-flint/loess interface ( $x, y, z$  are Cartesian coordinates,  $z$  directed upward). Because of its low intrinsic permeability, the clay-with-flint cover is close to saturation in spring. The thickness of the loess layer is noted  $e(x, y) = z(x, y) - h(x, y)$ . According to Aubert et al. [1990, 1991], the thickness of the vadose zone is related to the self-potential signals recorded at the ground surface  $\varphi(x, y)$  by

$$e(x, y) = \varphi(x, y)/c_V + (z_0 - h_0), \quad (1)$$

where  $e_0 \equiv z_0 - h_0$  is the thickness of the vadose zone below the reference electrode and  $c_V$  is an apparent voltage coupling coefficient expressed in mV/m. Equation (1) is the fundamental equation of the SPS model, but we will show in Appendix A that it can be derived from a more fundamental model. Aubert and Yéné Atangana [1996] named the interface determined from the self-potential signals according to equation (1) the “SPS surface.” The topography of this interface with reference to a fixed datum (e.g., the sea level) is described by

$$h(x, y) = z(x, y) - \varphi(P)/c_V - (z_0 - h_0). \quad (2)$$

According to Aubert and Yéné Atangana [1996], the SPS surface corresponds to the piezometric surface or to the elevation of the first impermeable formation. Valley-like depressions of the SPS surface correspond to preferential groundwater flow pathways, whereas ridges of the SPS surface correspond to watersheds. Various heuristic predictions based on this simple model have been demonstrated by M. Aubert and coworkers giving credit to this model among hydrogeologists.

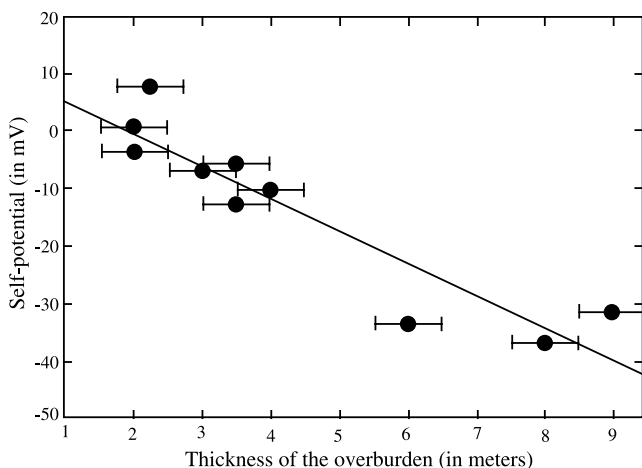


**Figure 7.** Correlation between the self-potential signals  $\varphi(P)$  and the thickness of the loess layer  $e(x, y)$  ( $R = 0.83$ ) (data from profile P1). The apparent voltage coupling coefficient  $c_V$  determined from the slope of this linear trend is equal to  $-5.7 \text{ mV m}^{-1}$ .

[17] As mentioned in section 2, the hydraulic conductivity of the clay layer is low ( $\sim 10^{-10} \text{ m s}^{-1}$ ) so this interface would correspond to the SPS surface because it corresponds to the elevation of the first impermeable formation. This idea is confirmed by the fact that during spring, shallow boreholes show the existence of superficial flow just above the clay with flint cover and during summer, we found the vadose zone in the loess cover as being very dry.

[18] To test this idea further, we performed several electrical resistivity surveys to capture the geometry of the system. One electrical tomogram is shown in Figure 6

together with a high-resolution self-potential survey made just after the resistivity survey. The position of this profile (named P1) is reported on Figures 1 and 2.

[19] To determine the apparent voltage coupling coefficient entering equation (2), we proceed as follows. A borehole was drilled on profile 1 (Figure 6). Using the lithological information from this drill hole (observation of the loess and clay with flint covers) and the resistivity profile (Figure 6), we extrapolate the interface between the loess and the clay layer using a resistivity value of  $28 \Omega\text{m}$  (dashed line in Figure 6). Then we plot the value of the self-potential signals as a function of the thickness of the loess layer for equally spaced points (Figure 7). We observed a relatively good linear relationship between self-potential values and the thickness of the loess layer. The apparent voltage coupling coefficient  $c_V$  determined from the slope of this trend, is equal to  $-5.7 \text{ mV m}^{-1}$  (Figure 7). Finally, we reconstructed the shape of the interface between the loess and the clay units using equation (2) and  $c_V = -5.7 \text{ mV m}^{-1}$  using the data from the spring 2005 survey. The final SPS surface is reported on Figure 8. We can observe the ridge along which the sinkholes are located. In addition, the position of the sinkholes themselves is clearly seen.

[20] In summer, few self-potential anomalies remain visible on the self-potential map (Figure 5b). The summer 2005 was very dry in France, and no superficial water flow was observed above the clay with flint cover into the boreholes. The variations of saturation and groundwater flow in the vadose zone of the loess layer between spring and summer explain the differences between the two self-potential surveys. Indeed, *Friedel et al.* [2004] and *Doussan et al.* [2002] have presented evidence that self-potential signals are influenced by the direction of groundwater flow in the vadose zone and total head and moisture distributions.

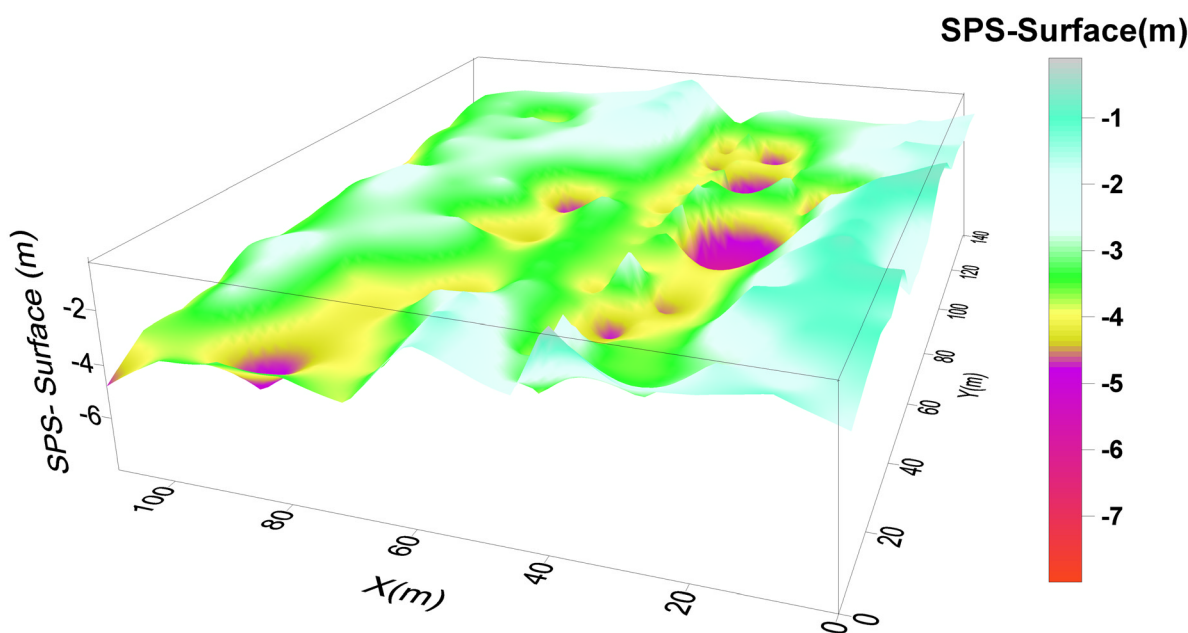


**Figure 8.** SPS map determined from the self-potential data for the spring data (Figure 5a) and the correlation between the self-potential signals and the thickness of the overburden (Figure 4). Note that the sinkholes are organized along a north-south trend.

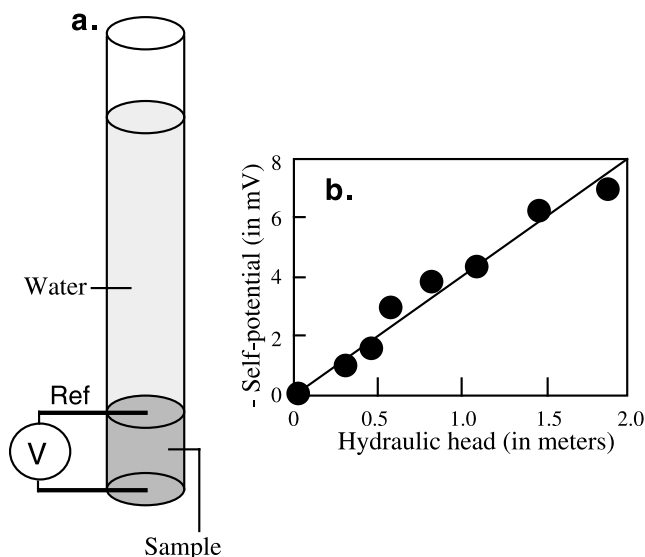


**Figure 9.** Determination of the streaming potential coupling coefficient of a sample. (a) Experimental setup. (b) Measurement of the self-potential signals as a function of the variations of the imposed hydraulic head difference through the core sample in steady state conditions. The slope of this trend yields the intrinsic value of the streaming potential coupling coefficient expressed in mV per meter of hydraulic head.

[21] We believe that differences between the two self-potential maps could be explained by evaporation differences between spring and summer and the smaller amount of precipitation in summer compared to the situation in spring. In summer, the moisture content in the loess layer is very low compared to the situation during spring. This is demonstrated by apparent resistivity surveys performed in March and in August using electromagnetic tools (EM31 and EM34). In addition, evaporation creates an additional source of positive self-potential signals that can counterbalance the contribution associated with the downward percolation of the meteoric water through the loess layer. While the SP measurements were found to be stable in spring, the self-potential measurements performed during a day in summer exhibit clear changes in the strength and sometimes polarity at different times during the day (few mV). We believe that daily variations of the self-potential data are related to evaporation, but clearly additional observations have to be made in this direction before reaching definite conclusions. In sections 4 and 5, we will focus only on the self-potential map made in spring 2005 in order to demonstrate the underlying physics of this process.

### 3.2. Laboratory Measurements of the Coupling Coefficient

[22] We believe that the mechanism responsible for the hydroelectric coupling reported in this work is the so-called streaming potential. The streaming potential is related to the drag of the excess of electrical charge contained in the pore water by the flow of the groundwater [Nourbehecht, 1963; Ishido and Mizutani, 1981]. To investigate the streaming potential polarization process, we performed laboratory measurements of the streaming potential coupling coefficient

of various samples collected at different depths in the loess and clay with flint covers. We determine the intrinsic streaming potential coupling coefficient with the experimental setup shown Figure 9. The intrinsic streaming potential coupling coefficient is determined from the ratio between the electrical potential difference measured at the end faces of the cylindrical sample and the applied hydraulic head difference. The resulting experimental estimation of the streaming potential coupling coefficient is reported in Table 1. Because the intrinsic streaming potential coupling coefficient depends on the electrical conductivity of the groundwater [e.g., Revil *et al.*, 1999, 2004, and references therein], it was necessary to sample the groundwater from the test site. We found a substantial difference between the mineralization and electrical conductivity of the groundwater sampled in the main aquifer located in the chalk ( $\sigma_f(25^\circ\text{C}) = 0.058 \text{ S m}^{-1}$  at a depth of  $\sim 32 \text{ m}$ ) and superficial water located above the clay with flint cover ( $\sigma_f(25^\circ\text{C}) = 0.029 \text{ S m}^{-1}$ ). Consequently, we performed our measurements with water sampled just above the clay with flint cover. In this work, we have assumed that the conductivity of the groundwater is homogeneous in the loess cover. Additional work will be needed to address this point and to determine the standard deviation associated with this parameter.

[23] Experiments were performed for three soil samples taken above the clay with flint layer. Results show an unexpected large range of values for the streaming potential coupling coefficient with an average value of  $-5 \pm 3 \text{ mV m}^{-1}$ . This average value is, however, very close to the value of the apparent voltage coupling coefficient reported in section 3.1 ( $c_V = -5.7 \text{ mV m}^{-1}$ ). The apparent voltage coefficient at the field scale is probably more accurate because it averages over a larger volume. The similarity implies that the self-potential signals recorded at the test site can be interpreted as a streaming potential. We further develop this point in section 4 by modeling the coupled hydroelectric problem in this type of environment using a finite element code.

## 4. Numerical Modeling

[24] In this section, we look for a fundamental understanding of the coupled hydroelectric coupling problem to explain the shape and strength of the self-potential anomalies observed during the spring survey. In section 4.1, we recall the equations for the head distribution in steady state conditions and the resulting distribution for the electrical potential owing to the streaming potential coupling.

### 4.1. Theoretical Framework

[25] In a water-saturated porous soil, there is always an excess of electrical charge located in the vicinity of the pore

**Table 1.** Measurement of the Streaming Potential Coupling Coefficient  $C$  and Electrical Resistivity  $\rho$  at a Frequency of a Few Kilohertz

Samples	Depth, m	$\sigma_f(25^\circ\text{C}), \text{ S m}^{-1}$	$C, \text{ mV m}^{-1}$	$\rho, \Omega \text{ m}$	$L, \text{ A m}^{-2}$
S1-1	2.5	0.0283	$-4.0 \pm 0.6$	61	$6.6 \times 10^{-5}$
S1-2	5.5	0.0283	$-2.1 \pm 0.6$	73	$2.7 \times 10^{-5}$
S1-3	11.7	0.0351	$-10 \pm 2$	23	$4.3 \times 10^{-4}$

**Table 2.** Material Properties Used for the Numerical Model<sup>a</sup>

Material	$K, \text{ m s}^{-1}$	$\rho, \Omega \text{ m}$	$L, \text{ A m}^{-2}$
Loess	$10^{-9}$	77	$8.5 \times 10^{-5}$
Clay with flint	$10^{-10}$	10	$9.8 \times 10^{-5}$
Chalk	$10^{-10}$	80	$9.8 \times 10^{-5}$
Sinkhole	$10^{-8}$	60	$8.5 \times 10^{-5}$

<sup>a</sup>The resistivity values are taken from the resistivity survey at a frequency of few hertz.

water mineral interface. The drag of this excess of charge, by the flow of the groundwater, is responsible for a net source of electrical current. The total electrical current density  $\mathbf{j}$  ( $\text{A m}^{-2}$ ) is related to the hydraulic head  $h$  (m) by the following constitutive equation [e.g., *Sill*, 1983; *Fournier*, 1989]:

$$\mathbf{j} = -\sigma \nabla \varphi - L \nabla h, \quad (3)$$

where the current coupling coefficient  $L$  (expressed in  $\text{A m}^{-2}$ ) characterizes the electrical current density produced in response to the unit hydraulic gradient. The first term of the right-hand side of equation (3) represents the conduction current density (Ohm's law), and the second term corresponds to the streaming current density (source current). The voltage coupling coefficient  $C = -L/\sigma$  (in  $\text{V m}^{-1}$ ) characterizes the voltage drop in response to a unit hydraulic head gradient and corresponds therefore to the true streaming potential coupling coefficient reported in section 3.2.

[26] The continuity equation for the electrical charge is  $\nabla \cdot \mathbf{j} = 0$ , which means that  $\mathbf{j}$  is conservative in the quasi-static limit of the Maxwell equations. Combining equation (3) and the continuity equation yields the classical Poisson equation for the electrical potential,

$$\nabla \cdot (\sigma \nabla \varphi) = -\nabla \cdot (L \nabla h), \quad (4)$$

where the right-hand side corresponds to the source term associated with the hydraulic head distribution and heterogeneity in the distribution of the current coupling coefficient  $L$ . The self-potential distribution is therefore obtained by solving first the boundary value problem for

the hydraulic head. The field equation is obtained by combining the Darcy equation with the continuity equation for the mass of the pore water. In steady state conditions, the distribution of the hydraulic head is controlled by the distribution of the hydraulic conductivity and the boundary condition for the hydraulic head or the flux.

#### 4.2. Finite Element Modeling

[27] To determine the distribution of the electrical potential resulting from the percolation of the groundwater, we follow the methodology proposed by *Sill* [1983] more than 20 years ago. We first solve the hydraulic equation for the hydraulic head  $h(x, z)$  with appropriate boundary conditions, which are discussed below. Then, the right-hand part of equation (4) is computed with a given distribution of the current coupling coefficient  $L(x, z)$ . Finally, equation (4) is solved for  $\varphi(x, z)$  with a given distribution of the electrical conductivity  $\sigma(x, z)$ . The distribution of the electrical conductivity is approximated by the electrical resistivity tomogram of Figure 6. The values of the current coupling coefficient and hydraulic conductivity for each of the three lithological units (loess, clay, and chalk) are reported in Table 2. The geometry used for the computations is shown Figure 10. The interface between the loess and the clay layers is determined from the electrical resistivity tomogram of Figure 6, and the interface between the clay with flint cover and the chalk formation is assumed to be flat (we show below that the real geometry of this interface has no influence upon the distribution of the electrical potential at the ground surface).

[28] We use the finite element code FEMLAB to solve the hydroelectric boundary value problem. Meteoric water percolates uniformly downward in the loess layer. The boundary conditions are as follows. At the upper boundary  $\partial\Omega_2$ , we fixed the flux for the groundwater equal to the infiltration capacity of the sinkhole ( $10^{-7} \text{ m}^2 \text{ s}^{-1}$ , that is  $3 \text{ m yr}^{-1}$ ) because of the observed runoff of water in sinkholes in this area. At the upper boundary  $\partial\Omega_1$ , the hydraulic flux is set equal to the rain rate ( $0.6 \text{ m yr}^{-1}$ ), which is the mean rain rate measured in this area. The two opposite vertical sides of the system are characterized by impermeable boundary conditions,

$$\mathbf{n} \cdot \mathbf{u} = 0, \quad (5)$$

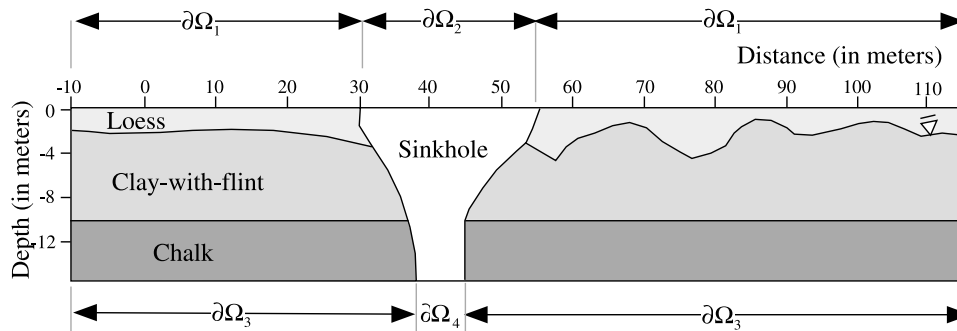


**Figure 10.** Geometrical model used for the finite element calculation. The geometry of the interface between the loess and the clay with flint formation is determined from the resistivity tomogram. The material properties used for the calculations are reported in Table 2, and the boundary conditions are discussed in the main text.

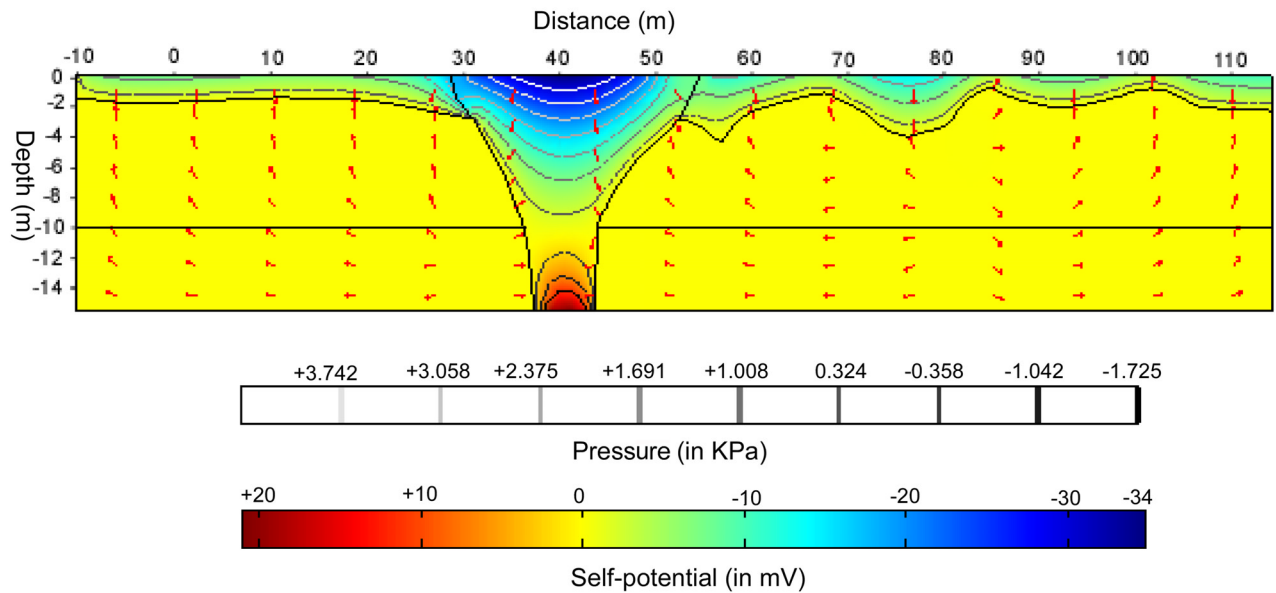


**Figure 11.** Self-potential distribution (in mV) calculated using the finite element numerical model FEMLAB. The contour lines show the pressure field (in kPa), while the arrows indicate the direction (not the strength) of the groundwater flow. The sinkhole is characterized by a dipolar anomaly, while the other self-potential anomalies indicate the thickness of the loess cover.

where  $\mathbf{n}$  is the outward unit vector normal to the boundary and  $\mathbf{u}$  is the Darcy flux. At the lower boundary  $\partial\Omega_4$ , we fixed the flux for the groundwater equal to the exfiltration capacity of the sinkhole. The lower boundary  $\partial\Omega_3$  is considered to be impermeable. For the electrical potential, we use the insulating boundary condition

$$\mathbf{n} \cdot \mathbf{j} = 0, \quad (6)$$

everywhere. An alternative choice would be to consider  $\psi \rightarrow 0$  at infinity (except at the ground surface where  $\mathbf{n} \cdot \mathbf{j} = 0$ ).

[29] The computed Darcy velocity is in the range  $(6-8) \times 10^{-6} \text{ m s}^{-1}$  in the loess and below  $10^{-11} \text{ m s}^{-1}$  in the clay with flint cover and in the chalk. The distribution of the electrical potential resulting from the distribution of the hydraulic heads is shown in Figure 11. There is a good agreement between the modeled and the measured SP data. There is a sharp variation in the hydraulic head gradient between the loess and the clay with flint covers because of the permeability distribution. As shown in Appendix A, this gradient is likely responsible for the shape of the self-potential anomalies observed at the ground surface. In the loess, the distribution of the equipotentials follows the shape of the interface between the loess and the clay formations. A comparison between the self-potential profile measured at the ground surface and the self-potential profile determined from the numerical model along the same profile is shown Figure 12. We observe a fairly good agreement between the model and the data without any optimization of the material properties and the geometry of the interface between the loess and the clay layers. Only the flux of the water percolating through the sinkhole was adjusted. This indicates clearly that outside the areas where the sinkholes are

located, the self-potential signals measured at the ground surface indicate the thickness of the loess cover and therefore the presence of ridges that can channel shallow groundwater flow into sinkholes. An explanation of this behavior, based on potential field theory, is given in Appendix A. The sinkholes themselves are characterized by dipolar self-potential signals (positive pole located at

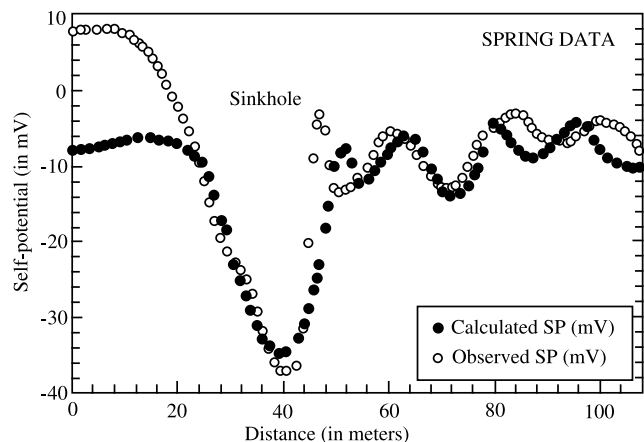


**Figure 12.** Comparison between the self-potential signals determined at the ground surface using the finite element model (see Figure 11) and the self-potential measurements performed along profile P1 (see position on Figures 1 and 2). We note a fairly good agreement between both profiles except at the beginning of the profile. The reference for the two profiles is taken at  $x = -10 \text{ m}$  (see Figure 11). Some of the variation between the observed and predicted curves could come from lateral heterogeneity in the loess cover.

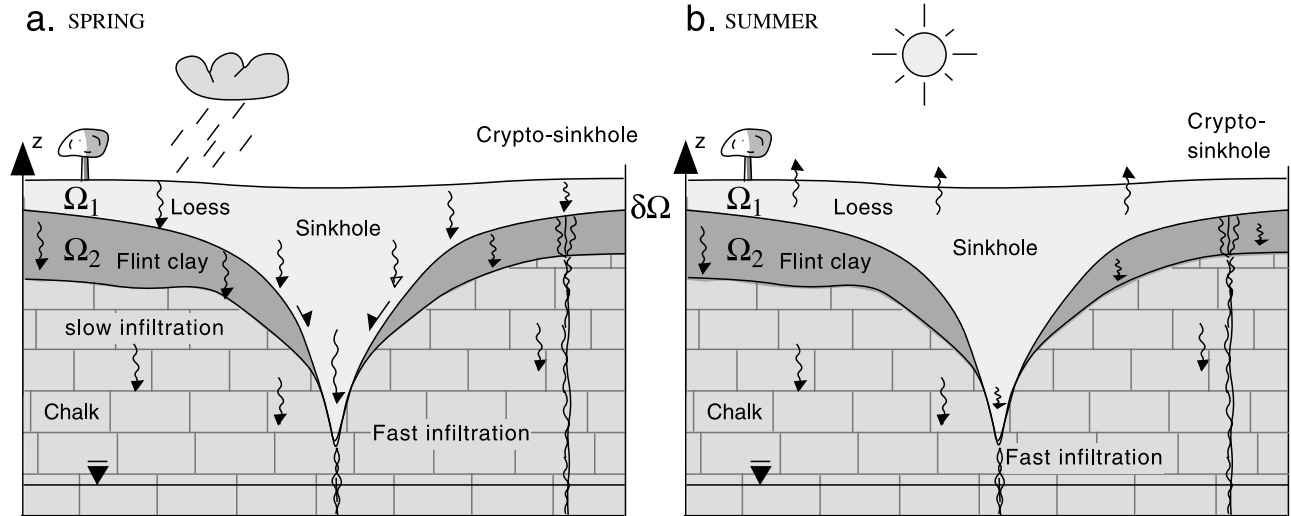


**Figure 13.** Interpretation of the self-potential changes between spring and summer. (a) In spring, large negative self-potential anomalies are associated with percolation of the groundwater in sinkholes. Smaller negative self-potential anomalies are associated with the existence of sinkholes. (b) In summer, small negative anomalies are still associated with the percolation of water in the main sinkholes, but no clear anomalies can be associated with the crypto-sinkholes. Evaporation is responsible for some positive self-potential signals at the ground surface.

depth when the reference is taken at infinite). It follows that the self-potential fingerprint of the sinkholes and crypto-sinkholes is a negative anomaly (the negative pole is located close to the ground surface and the positive pole is likely located close to the top of the chalk formation). The self-potential signatures of the sinkholes are related to the flux of water passing through them. This also explains why there is a change in SP data between spring and summer (Figure 13).

## 5. Tomography

[30] In this section, we provide algorithms to analyze quantitatively the self-potential signals in terms of source location and geometry of the source body. As discussed above, the recorded self-potential map evidences the superposition of two signals. The first one is associated with the loess/clay with flint interface and is characterized by a dipolar distribution of charge located along this interface. The second distribution is associated with the percolation of water in the sinkholes. In this case, each sinkhole can be seen as a single dipole, and the depth of this dipole is approximately half the distance between the ground surface and the chalk formation. We first apply a tomography algorithm to locate the depth of the sinkholes.

### 5.1. Tomography of the Sinkholes

[31] Self-potential tomography was introduced by *Patella* [1997a, 1997b]. However, his algorithm was restricted to monopole charge accumulations. To locate the position of a distribution of individual dipoles that would correspond to the SP signature of the percolation of water through the sinkholes, we rely here on a generalization of the 2-D dipolar occurrence probability (DOP) algorithm developed by *Revil et al.* [2003b]. *Iuliano et al.* [2002] proposed a 3-D

version of the DOP. We consider a Cartesian coordinate system  $(x, y, z)$  with the  $z$  axis positive downward. We assume that the electrical field  $\mathbf{E}(\mathbf{r})$  is due to  $P$  dipoles with moment  $\mathbf{d}_p$  ( $p \in \{1, 2, \dots, P\}$ ) and is therefore given by

$$\mathbf{E}(\mathbf{r}) = \sum_{p=1}^P (\mathbf{d}_p \nabla_p) s(\mathbf{r}_p - \mathbf{r}), \quad (7)$$

$$s(\mathbf{r}_p - \mathbf{r}) = \frac{\mathbf{r}_p - \mathbf{r}}{|\mathbf{r}_p - \mathbf{r}|^3}. \quad (8)$$

We note  $E$  the modulus of the electrical field  $\mathbf{E}(\mathbf{r})$ . The power associated with the electrical field is

$$\varphi(E) = \int_S E^2(\mathbf{r}) dS, \quad (9)$$

$$\varphi(E) = \sum_{p=1}^P \sum_v d_{p,v} \int_S \mathbf{E}(\mathbf{r}) \frac{\partial s(\mathbf{r}_p - \mathbf{r})}{\partial v_p} dS. \quad (10)$$

We assume that the projection of  $S$  onto the  $(x, y)$  horizontal plane can be adapted to a rectangle with side  $X$  and  $Y$  along the  $x$  and  $y$  axis, respectively. We note  $g(z)$  the topography regularization factor, which is defined by

$$g(z) = \left[ 1 + \left( \frac{\partial z}{\partial x} \right)^2 + \left( \frac{\partial z}{\partial y} \right)^2 \right]^{1/2}, \quad (11)$$

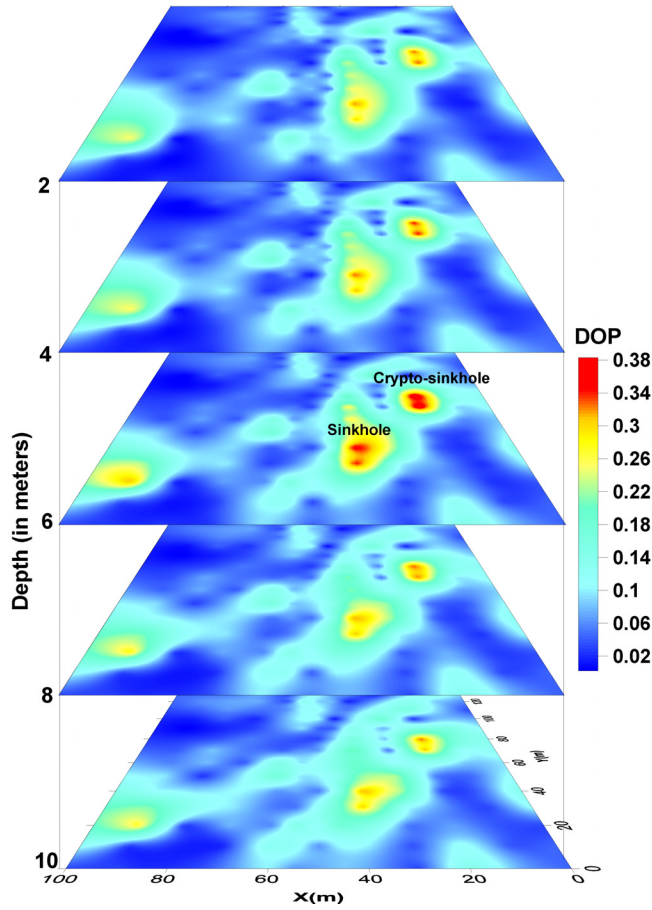


**Figure 14.** Dipole occurrence probability (DOP) responsible for the self-potential anomaly associated with percolation of water in the sinkholes. The maximum of the DOP is found at a depth of 6 meters. This depth corresponds to half the depth of the chalk formation.

and in absence of topography,  $g(z) = 1$ . Applying Schwarz's inequality, *Iuliano et al.* [2002] defined a source dipole occurrence probability (SDOP),

$$\eta_v(r_p) = C_v^p \int_{-X}^X \int_{-Y}^Y \mathbf{E}(\mathbf{r}) \frac{\partial \mathbf{s}(\mathbf{r}_p - \mathbf{r})}{\partial v_p} g(z) dx dy \quad (12)$$

where  $v = x, y, z$ ,  $v_p = x_p, y_p, z_p$  and where the normalization constant  $C_v^p$  is defined by

$$C_v^p = \left[ \int_{-X}^X \int_{-Y}^Y E^2(\mathbf{r}) g(z) dx dy \int_{-X}^X \int_{-Y}^Y \left| \frac{\partial \mathbf{s}(\mathbf{r}_p - \mathbf{r})}{\partial v_p} \right|^2 g(z) dx dy \right]^{-1/2} \quad (13)$$

The DOP function represents therefore the probability of finding in a point of the subspace  $\Omega$  a dipole responsible for the self-potential anomaly observed at the ground surface. Note that in our case, the dipolar momentum will be generally directed downward because of the percolation of the groundwater. The position of the dipole would be half of

the distance between the ground surface and the chalk substratum. A tomography of the self-potential signals is shown in Figure 14. According to the tomography algorithm, the position of the dipole responsible for the observed SP anomaly is located at a depth of  $6 \pm 2$  m. The position of the chalk substratum, determined from the electrical resistivity tomogram, is at a depth of  $11 \pm 1$  m. This is consistent with our model.

## 5.2. Tomography of the Loess/Clay Interface

[32] We look first to recover the loess/clay interface using the self-potential measurements made at the ground surface along profile P1. Equation (A5) of Appendix A indicates that the loess/clay interface behaves as a sum of dipoles, each dipole with a strength proportional to the elevation of the interface above a datum. Therefore it should be possible, in principle, to deconvolve the self-potential signals recorded at the ground surface to find the location of these dipoles in the ground and therefore to image the interface between the loess cover and the clay with flint cover. For a 3-D profile, the electrical potential at the point P located at the ground surface is given by

$$\varphi(P) = \frac{\delta C}{2\pi} \int_{\partial\Omega} h \frac{\mathbf{x} \cdot \mathbf{n}}{x^3} dS, \quad (14)$$

where  $\mathbf{x} = \mathbf{r} - \mathbf{r}'$  and  $x = |\mathbf{x}|$ ,  $x \equiv MP$ ,  $\mathbf{n}$  is the outward normal to the clay/loess interface at the source point M,  $dS$  is a surface element of the clay/loess interface around M,  $h$  is the hydraulic head at source point M, and  $\delta C = C_2 - C_1$  is the difference of the streaming potential coupling coefficient through the loess/clay interface. To invert equation (14), we generalize the cross-correlation algorithm developed by *Revil et al.* [2003a]. Isovalues of the final  $\alpha$ -normalized distribution defined by *Revil et al.* [2003a] are contoured to provide a tomographic image of all the possible locations of the loess/clay interface. The solution is therefore nonunique, and there is an infinity of interfaces that would be responsible for the same self-potential distribution. To

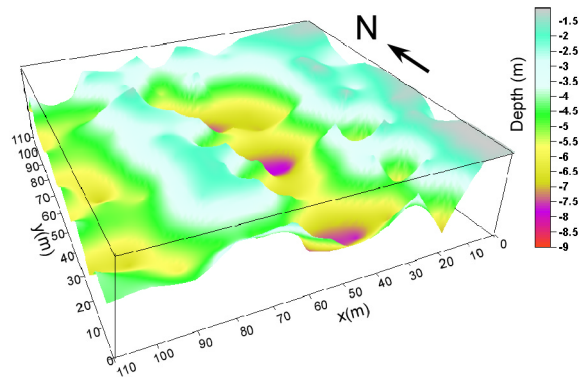


**Figure 15.** Determination of the topography of the loess/clay with flint interface (the colors code the depth of this interface, expressed in meters). Note that the maximum of the depth of this interface coincides with the depth of the chalk formation (8 to 12 m).

reduce the nonuniqueness of the problem, the position of the loess/clay with flint interface is known at a given location (in a borehole) and then can be extrapolated everywhere assuming that the electrokinetic conversion factor  $\delta C$  is the same in the investigated area at the scale of the measurements. We applied such a tomographic algorithm to the self-potential data of spring 2005. Using the data of wells W1 and W2 (Figures 1 and 2), the inverted position of the clay/loess interface is shown Figure 15.

## 6. Concluding Statements

[33] The self-potential method indicates the position of sinkholes and crypto-sinkholes in a chalk formation in Normandy demonstrating the usefulness of this method in delineating a series of sinkholes located along two ridges and the position of the clay with flint/loess interface. The negative self-potential signals are associated with downward percolation of the meteoritic water between the ground surface and the clay-with-flint formation. Outside the sinkholes, the self-potential signals show a fairly good linear correlation to the thickness of the permeable loess layer. This is explained by the distribution of the head in the loess and clay with flint covers. A finite element model is used to compute the self-potential signals resulting from groundwater flow. A fairly good agreement is obtained between the computed and the measured self-potential signals. Finally, we proposed two three-dimensional tomography algorithms (1) to reconstruct the interface between the loess and the clay with flint covers and the position of the sinkholes and (2) to locate the extension of the sinkholes at depth.

## Appendix A: A Physical Model of the SPS Method

[34] We look here for a physical link between the forward numerical model developed in section 4 and the SPS method discussed in section 3.1. Introducing an effective potential,  $\psi \equiv \varphi - C'h$ , the boundary value problem described in section 4 is [Fournier, 1989; Santos et al., 2002]

$$\nabla^2 \psi = 0, \mathbf{r} \in \Omega_{1,2}, \quad (\text{A1})$$

$$\sigma_1 \mathbf{n} \cdot \nabla \psi_1 = \sigma_2 \mathbf{n} \cdot \nabla \psi_2, \mathbf{r} \in \partial\Omega, \quad (\text{A2})$$

$$\psi_2 - \psi_1 = -(C_2 - C_1)h, \mathbf{r} \in \partial\Omega, \quad (\text{A3})$$

as  $\varphi$  and  $h$  are continuous across the interface between the clay with flint and loess covers and where  $\partial\Omega$  represents the interface between the loess (compartment  $\Omega_1$ ) and the clay with flint (compartment  $\Omega_2$ ). The effective potential  $\psi$  follows the Laplace equations in the volume  $\Omega_{1,2}$  while there is a drop in the effective potential across  $\partial\Omega$ . In addition, the normal component of the current density vanishes at the ground surface because the atmosphere is insulating ( $\mathbf{n} \cdot \nabla \varphi = 0$  at the ground surface).

[35] Using the image technique for finding the solution of the previous boundary value problem for a half-conducting

space, the effective potential at the observation P at the ground surface is

$$\psi(\mathbf{P}) = \int_{\partial\Omega} \nabla \left( \frac{1}{x} \right) \cdot \mathbf{P} dS, \quad (\text{A4})$$

where  $\mathbf{P} = [\delta C h / 2\pi] \mathbf{n}$  is the density of current dipole moment confined to the interface  $\partial\Omega$  at the observation station P,  $\mathbf{x} = \mathbf{r} - \mathbf{r}'$  and  $x = |\mathbf{x}|$ , and  $dS$  is a surface element of the interface  $\partial\Omega$ ,  $\mathbf{n}$  is the outward normal to the clay/loess interface at the source point M,  $x \equiv MP$ ,  $dS$  is a surface element of the clay/loess interface around M, and  $h$  is the hydraulic head at source point M, and  $\delta C = C_2 - C_1$  is the difference of the streaming potential coupling coefficient through the loess/clay interface. The electrical potential at observation point P is given by

$$\varphi(\mathbf{P}) = \frac{\delta C}{2\pi} \int_{\partial\Omega} h \frac{\mathbf{x} \cdot \mathbf{n}}{x^3} dS. \quad (\text{A5})$$

Equation (A5) can be simplified as the interface  $\partial\Omega$  is seen from the observation point P with a solid angle equal to  $2\pi$ , then a first-order solution of equation (A5) is  $\varphi(\mathbf{P}) - \varphi_0 \approx \delta C(h - h_0)$ , and therefore we recover equation (1) of the main text.

[36] **Acknowledgments.** We thank the University of Rouen, the CNRS, and IRIS instrument for their support. We thank C. Gioia, T. Leboulanger, J. Grandsir, and M. Simon for their help in the field and L. Bentley for his scientific advice. We also thank the Associate Editor and the two referees for their helpful reviews of our manuscript.

## References

- Ahmed, S., and P. J. Carpenter (2003), Geophysical response of filled sinkholes, soil pipes and associated bedrock fractures in thinly mantled karst, east-central Illinois, *Environ. Geol.*, *44*, 705–716.
- Aubert, M., and Q. Yéné Atangana (1996), Self-potential method in hydrogeological exploration of volcanic areas, *Ground Water*, *34*, 1010–1016.
- Aubert, M., I. N. Dana, and M. Livet (1990), Vérification de limites de nappe aquifères en terrain volcanique par la méthode de polarisation spontanée, *C. R. Acad. Sci., Ser. II*, *311*, 999–1004.
- Aubert, M., I. N. Dana, and J. C. Dupuy (1991), Application de la méthode de polarisation spontanée à la découverte des circulations d'eau souterraine en terrain volcanique, *C. R. Acad. Sci., Ser. II*, *312*, 325–330.
- Boubekraoui, S., and M. Aubert (1999), Self-potential method applied to the geological and hydrogeological investigation of shallow structures at Grand-Brûlé (Réunion Island, Indian Ocean) (in French), *Hydrogeologie*, *1*, 43–51.
- Brouyères, S., A. Dassargues, and V. Hallet (2004), Migration of contaminants through the unsaturated zone overlying the Hesbaye chalky aquifer in Belgium: A field investigation, *J. Contam. Hydrol.*, *72*, 135–164.
- Closson, D., N. A. Karaki, M. J. Hussein, H. Al-Fugha, A. Ozer, and A. Mubarak (2003), Subsidence et effondrements le long du littoral jordanien de la mer Morte: Apport de la gravimétrie et de l'interférométrie radar différentielle, *C. R. Geosci.*, *335*, 869–879.
- Corwin, R. F., and D. B. Hoover (1979), The self-potential method in geothermal exploration, *Geophysics*, *44*(2), 226–245.
- Doussan, C., L. Jouniaux, and J.-L. Thony (2002), Variations of self-potential and unsaturated water flow with time in sandy loam and clay loam soils, *J. Hydrol.*, *267*, 173–185.
- Finizola, A., S. Sortino, J.-F. Lénat, and M. Valenza (2002), Fluid circulation at Stromboli volcano (Aeolian Islands, Italy) from self-potential and CO<sub>2</sub> surveys, *J. Volcanol. Geotherm. Res.*, *116*, 1–18.
- Finizola, A., S. Sortino, J.-F. Lénat, M. Aubert, M. Ripepe, and M. Valenza (2003), The summit hydrothermal system of Stromboli: New insights from self-potential, temperature, CO<sub>2</sub> and fumarolic fluid measurements. Structural and monitoring implications, *Bull. Volcanol.*, *65*, 486–504, doi:10.1007/s00445-003-0276-z.

- Fournier, C. (1989), Spontaneous potentials and resistivity surveys applied to hydrogeology in a volcanic area: Case history of the Chaîne des Puys (Puy-de-Dôme, France), *Geophys. Prospect.*, *37*, 647–668.
- Friedel, S., S. Byrdina, V. Jacobsa, and M. Zimmer (2004), Self-potential and ground temperature at Merapi volcano prior to its crisis in the rainy season 2000–2001, *J. Volcanol. Geotherm. Res.*, *134*, 149–168.
- Gex, P. (1977), La Méthode de Potentiel Spontané. Essai de Réhabilitation, thèse de Doctorat d'Etat, Univ. de Lausanne, Lausanne, France.
- Gurk, M., and F. P. Bosch (2001), Cave detection using self-potential-surface (SPS) technique on a karstic terrain in Jura mountains (Switzerland), in *Proceedings of the Meeting "Electrotromagnetische Tiefenforschung", 9–13 March, 2001*, edited by A. Hoerdet and J. Stoll, paper 19, Dtsch. Geophys. Ges., Leipzig, Germany.
- Ishido, T., and H. Mizutani (1981), Experimental and theoretical basis of electrokinetic phenomena in rock-water systems and its application to geophysics, *J. Geophys. Res.*, *86*, 1763–1775.
- Iuliano, T., P. Mauriello, and D. Patella (2002), Looking inside Mount Vesuvius by potential fields integrated probability tomographies, *J. Volcanol. Geotherm. Res.*, *113*, 363–378.
- Jackson, D. B., and J. Kauahikaua (1987), Regional self-potential anomalies at Kilauea Volcano, *U.S. Geol. Surv. Prof. Pap.*, *1350*, 947–959.
- Laïgnel, B., E. Dupuis, J. Rodet, M. Lacroix, and N. Massei (2004), An example of sedimentary filling in the chalk karst of the Western Paris Basin: Characterization, origins, and hydrosedimentary behaviour, *Z. F. Geomorphol.*, *48*(2), 219–243.
- Lange, A. L. (1999), Geophysical studies at Kartchner Caverns State Park, Arizona, *J. Cave Karst Stud.*, *61*(2), 68–72.
- Loke, M. H., and R. D. Barker (1996), Rapid least-squares inversion of apparent resistivity pseudosections by a quasi-Newton method, *Geophys. Prospect.*, *44*, 131–152.
- Nourbehecht, B. (1963), Irreversible thermodynamic effects in inhomogeneous media and their application in certain geoelectric problems, Ph.D. thesis, Mass. Inst. of Technol., Cambridge.
- Panno, S. V., and W. R. Kelly (2004), Nitrate and herbicide loading in two groundwater basins of Illinois' sinkhole plain, *J. Hydrol.*, *290*, 229–242.
- Patella, D. (1997a), Introduction to ground surface self-potential tomography, *Geophys. Prospect.*, *45*, 653–681.
- Patella, D. (1997b), Self-potential global tomography including topographic effects, *Geophys. Prospect.*, *45*, 843–863.
- Revil, A., P. A. Pezard, and P. W. J. Glover (1999), Streaming potential in porous media: 1. Theory of the zeta-potential, *J. Geophys. Res.*, *104*, 20,021–20,031.
- Revil, A., L. Ehouarne, and E. Thyreault (2001), Tomography of self-potential anomalies of electrochemical nature, *Geophys. Res. Lett.*, *28*(23), 4363–4366.
- Revil, A., V. Naudet, J. Nouzaret, and M. Pessel (2003a), Principles of electrography applied to self-potential electrokinetic sources and hydrogeological applications, *Water Resour. Res.*, *39*(5), 1114, doi:10.1029/2001WR000916.
- Revil, A., G. Saracco, and P. Labazuy (2003b), The volcano-electric effect, *J. Geophys. Res.*, *108*(B5), 2251, doi:10.1029/2002JB001835.
- Revil, A., V. Naudet, and J. D. Meunier (2004), The hydroelectric problem of porous rocks: Inversion of the water table from self-potential data, *Geophys. J. Int.*, *159*, 435–444.
- Santos, F. A. M., E. P. Almeda, R. Castro, R. Nolasco, and L. Mendes-Victor (2002), A hydrogeological investigation using EM34 and SP surveys, *Earth Planets Space*, *54*, 655–662.
- Sill, W. R. (1983), Self-potential modeling from primary flows, *Geophysics*, *48*(1), 76–86.
- van Schoor, M. (2002), Detection of sinkholes using 2D electrical resistivity imaging, *J. Appl. Geophys.*, *50*, 393–399.
- Zablocki, C. J. (1978), Streaming potentials resulting from the descent of meteoric water. A possible source mechanism for Kilauean self-potential anomalies, *Geotherm. Res. Trans.*, *2*(2), 747–748.
- Zhang, G.-B., and M. Aubert (2003), Quantitative interpretation of self-potential anomalies in hydrogeological exploration of volcanic areas: A new approach, *Near Surface Geophys.*, *1*, 69–75.

J. P. Dupont and A. Jardani, CNRS, Université de Rouen, UMR 6143 Morphodynamique Continentale et Cotière, Département de Géologie, Rouen, France.

A. Revil, Equipe Hydrogéophysique et Milieux Poreux, CNRS, CEREGE, Université Paul Cézanne (Aix-Marseille III), UMR 6635, F-13545, Aix-en-Provence, France. (revil@cerege.fr)